

Elongational Flow Induced Ordering in Surfactant Micelles and Mesophases

J. Penfold,^{*,†} E. Staples,[†] I. Tucker,[‡] P. Carroll,[‡] I. Clayton,[‡] J. S. Cowan,[‡] G. Lawton,[‡] S. Amin,[‡] A. Ferrante,[‡] and N. Ruddock[‡]

ISIS, Rutherford Appleton Laboratory, Chilton, Didcot, Oxon, U.K., and Unilever Research and Development, Port Sunlight Laboratory, Quarry Road East, Bebington, Wirral, U.K.

Received: March 4, 2005; In Final Form: September 30, 2005

We have used small angle neutron scattering, SANS, to investigate the elongational flow induced ordering in surfactant micelles and mesophases. Spatially resolved SANS measurements have been used to determine the distribution of orientational ordering over the flow velocity pattern in an elongational flow cell, and comparison with the effects of shear flow are made. Two different surfactant systems have been studied, the charged wormlike mixed micelles of hexaethylene monododecyl ether, C₁₆E₆/hexadecyl trimethylammonium bromide, C₁₆TAB (3% C₁₆E₆/5 mol % C₁₆TAB), and the L_α lamellar phase of C₁₆E₆ (50.6 wt % C₁₆E₆ at 55 °C), and a substantially different response is observed. The orientational distribution of the L_α lamellar phase of C₁₆E₆ reflects the flow velocity pattern distribution within the cell, whereas for the wormlike mixed micelles of C₁₆E₆/C₁₆TAB this is not the case, and this is associated with the shear thinning behavior of that system.

Introduction

The investigation of shear induced structures and transformations in soft matter is an important and growing field, and a number of excellent recent reviews exist.^{1,2} Phenomena observed include the simple alignment of rodlike particles, leading to shear thinning and shear thickening behavior, shear induced lamellar ordering and lamellar-to-vesicle transitions, shear induced crystallization, and shear banding (macroscopic shear induced phase separation). The relationship between microstructure and rheological properties in the context of flow processing is a particularly important aspect³ and covers a wide range of industrial process engineering applications, in fields as diverse as food processing, polymers, minerals, and detergent based products. Much of the original pioneering work used optical birefringence⁴ to probe microstructure, but in recent years, both X-ray^{5,6} and neutron scattering^{7–9} have been exploited. Predominantly, shear flow, established in Couette, cone and plate, or Poiseuille flow geometries, has been used, and relatively little attention has been focused on extensional or elongational flow. However, extensional flow is present in many commonly used flow geometries, in extruders and in pipe flow.

The development of elongational flow cells originates from the original work by Taylor¹⁰ on the four-roll mill and its subsequent exploitation by Odell et al.¹¹ in optical birefringence studies on polymers. More recently, X-ray and neutron scattering techniques have been used to study mixed shear-elongational flow effects in polymer melts in extruders,¹² in drawn polymeric sheets or fibers,⁶ and on an extruded thread of a surfactant hexagonal phase.¹³ An alternative geometry for approximating to an extensional flow field is opposed jets,¹⁴ and this has been exploited recently in both rheological¹⁵ and optical¹⁶ studies of polymer–surfactant mixtures. The crossed-slot geometry¹⁷ is particularly appealing because of its simplicity and adaptability for techniques such as X-ray and neutron scattering. This was demonstrated in the pioneering work of Idziak et al.,¹⁸ who

developed an extensional flow cell based on the crossed-slot geometry that was suitable for X-ray scattering studies. In some elegant experiments,^{5,18} they demonstrated how a fine X-ray beam could be used to map out the microstructure over the flow distribution within the cell. In particular, in addition to investigating the response to the flow pattern, they were able to show how low elongational flow rates can modify the lamellar spacing in undulating lamellar structures.⁵ Bent et al.¹² also demonstrated the use of small angle neutron scattering, SANS, to spatially resolve the microstructure on the millimeter length scale in their study of polymer blends in an extruder. The development of microfocus techniques on X-ray synchrotron sources¹⁹ has provided the opportunity for even finer spatial resolution.

Here, spatially resolved SANS measurements are used to investigate solution microstructure over the flow velocity pattern within an elongational flow cell. Two different systems are studied, the mixed surfactant wormlike micelles of C₁₆E₆/C₁₆TAB (3% C₁₆E₆/5 mol % C₁₆TAB) and the L_α lamellar phase of C₁₆E₆ (50.6 wt % C₁₆E₆ at 55 °C). The different flow induced ordering and changes in aggregation of these different microstructures are contrasted, and comparisons between the effects of shear and elongational flow are made. The construction of the elongational flow cell, based on the crossed-slot geometry and designed specifically for SANS measurements, is briefly described.

Experimental Details

(i) Elongational Flow Cell. The design of the elongational flow cell was inspired by the crossed-slot geometry flow cell designed for X-ray scattering by Idziak et al.¹⁸ The advantages of neutrons over X-rays for such a cell are that a combination of longer path length and thicker rigid windows make for better defined flow regimes. The design criteria for neutrons are sufficiently different from those for X-rays, that the construction of the cell is shown in Figure 1 and summarized in detail below.

The front and rear sections were made from 170 mm² pieces of 10 mm thick 316 stainless steel plate. Neutron transparent

[†] Rutherford Appleton Laboratory.

[‡] Port Sunlight Laboratory.

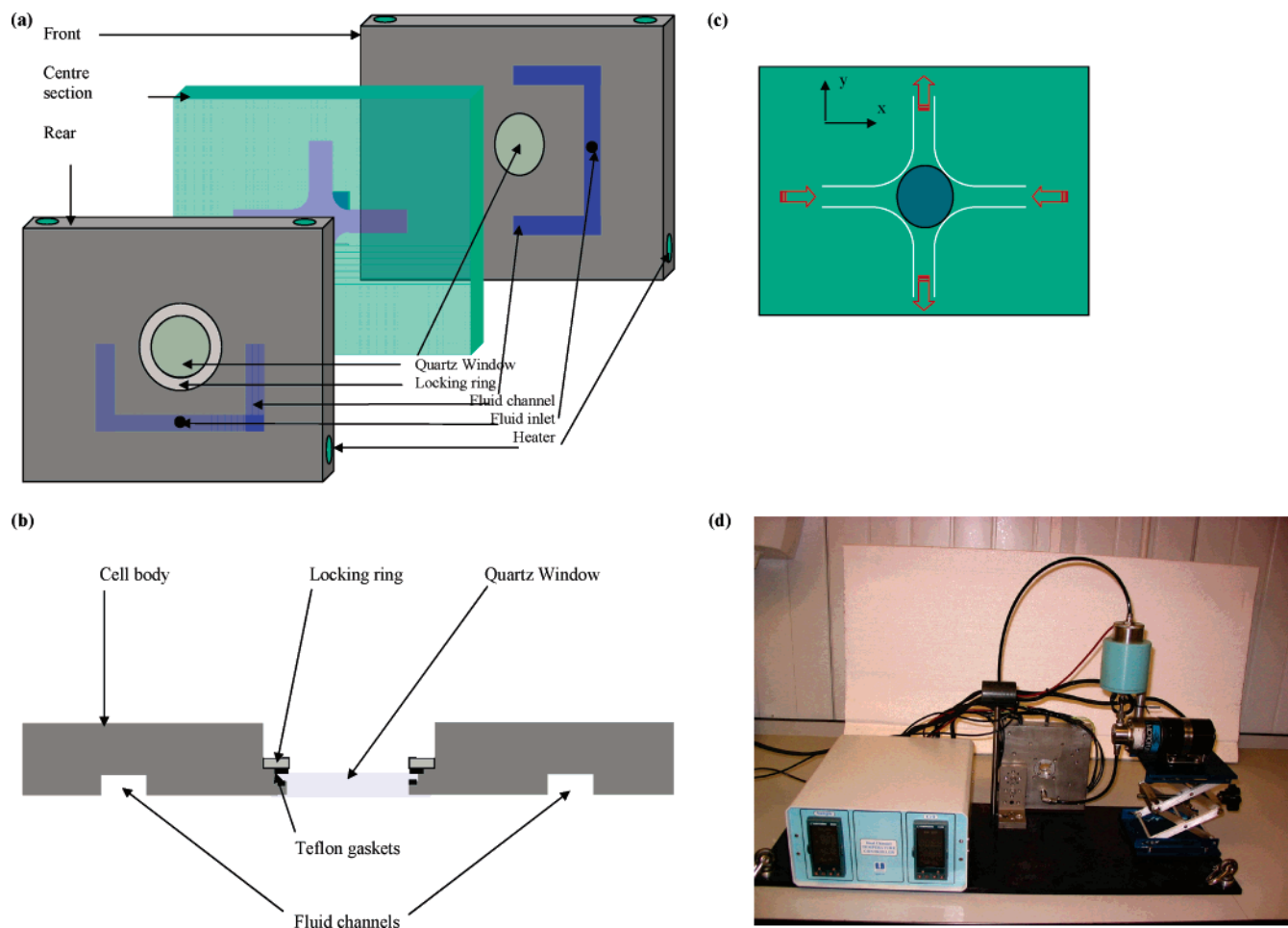


Figure 1. Elongational flow cell: (a) sketch of the cell showing construction with three coplanar plates; (b) close-up of the quartz window design; (c) cross-channel flow directions and coordinates; (d) photograph of the flow cell assembly.

windows (22 mm external diameter, 20 mm internal diameter, and 1.5 mm thickness) machined from Spectrosil quartz were centrally mounted into these plates from the outside surface. Window gaskets were cut from 300 μm Teflon sheets (Figure 1b). The depth of the windows in the plates was machined such that the inner surfaces of the window and steel plate were coplanar. The channels in the front and rear sections delivering fluid to the crossed slots were 11 mm wide and 2.5 mm deep. The center plate had a matching central cutout, and each vertex was rounded with an external radius to promote laminar flow adjacent to the neck point. Three separate central plates were made, with thicknesses of 2.5, 5, and 10 mm, for different total path lengths. Each plate had a 4 mm diameter, 10 mm deep hole to house a ceramic PT100 thermocouple. Cartridge heaters (5 mm) were mounted into the front and rear sections (240 V, 50 W) and connected in series to provide up to 100 W of heating. Two Eurotherm 2408 PID controllers were used with a common voltage set point to control the temperature of both the cell and a separate liquid reservoir. Heating rates were kept at 5 $^{\circ}\text{C}/\text{min}$ to minimize thermal stress on the windows. The entire assembly was mounted on an aluminum tooling plate piece, 1200 mm in length and 360 mm in depth. A Cole-Palmer Micropump (gear pump) was connected to the cell inlet using 4 mm internal diameter, 6 mm external diameter Teflon tubing. The outlet was returned to the reservoir above the pump, which also primed the pump via the same tubing. The total dead volume in the system with pipes, pump, and cell was approximately 35 mL. Power was supplied to the pump via a computer controlled Thurlby-Thamdar EX355P dc power supply.

The elongational flow is characterized by an extension rate, ϵ' , which represents the velocity gradient along the flow direction; that is, $\epsilon' = d v_y / d y$. In a thick cell, the effects of the walls can be ignored and pure elongational flow is observed. The maximum extensional rate can be expressed in terms of the volume flow rate, Q , and the slit dimensions,¹⁷ such that,

$$\epsilon' = Q / (w^2 t) \quad (1)$$

where w is the slit width and t is the slit depth. For our geometry, $w \sim 1$ cm and $t \sim 0.5$ cm, and thus, $\epsilon' \approx 2Q \text{ s}^{-1}$. The flow rates were calibrated for each of the samples studied by directly measuring the volume displacement. For a simple Newtonian fluid, the flow velocity between the walls is expected to have a Poiseuille-like distribution, with zero flow velocity at the walls and a maximum at the cell center, and this has been measured and reported by Idziak et al.¹⁸ Given the finite width and depth of the channels, in the central region, the flow regime will not be purely extensional and there will be a finite shear component. The Poiseuille-like flow distribution will give rise to a shear gradient in the z direction, with a maximum shear rate, $\gamma' (d v_y / dz)$, at the walls and zero at the center, and this has been considered in detail by Idziak et al.¹⁸ Given the larger channel depth, z (beam path length), of 5 mm compared to $\sim 1\text{--}2.5$ mm for X-rays, its effects here will be less significant but nevertheless finite. Assuming Poiseuille flow, the average shear rate will be $G \sim 5Q \text{ s}^{-1}$. An important design feature of this cell is the coplanar nature of the windows and flow channels. This will

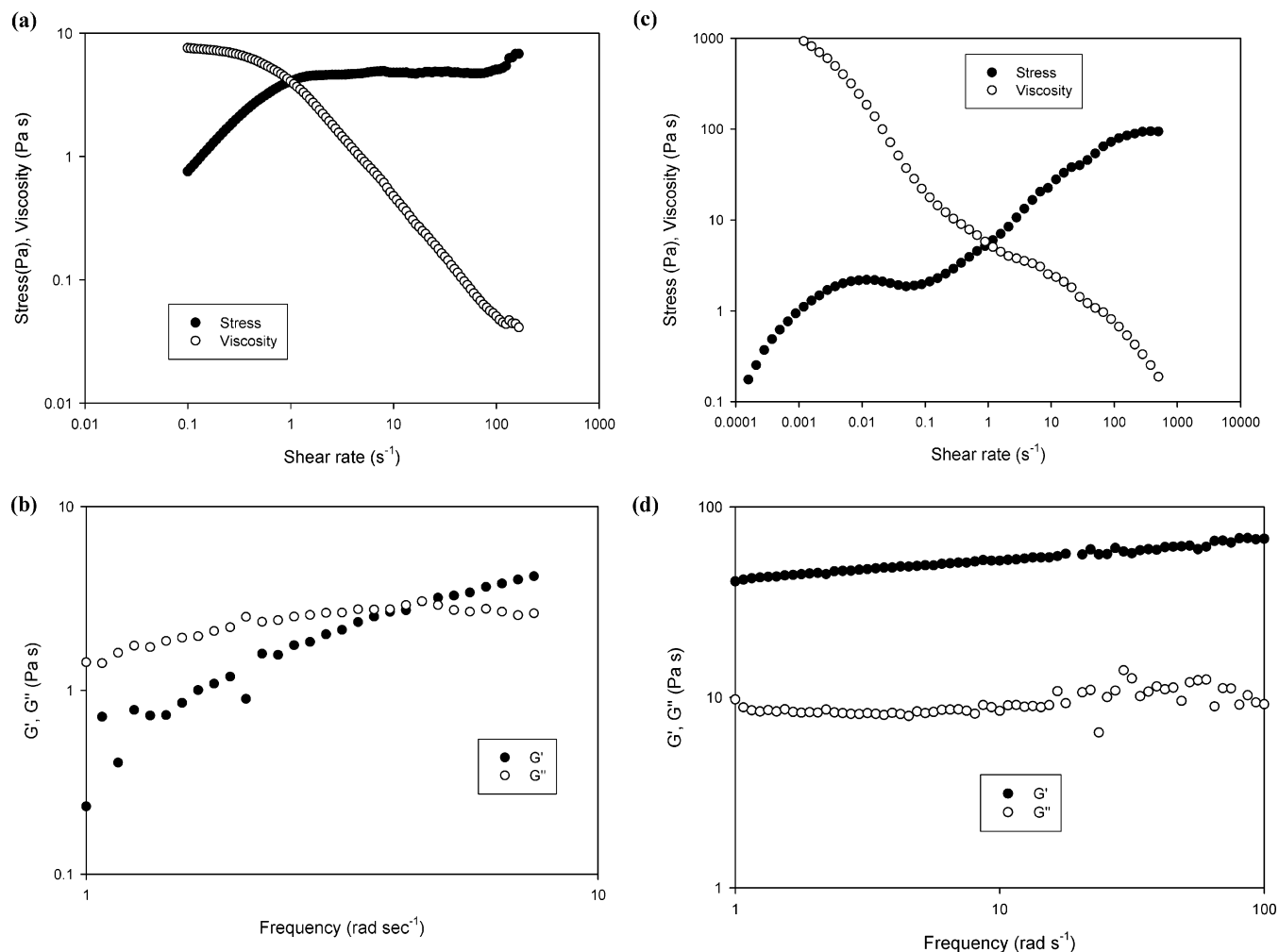


Figure 2. (a) Stress (Pa), viscosity (Pa s) dependence on shear rate (s⁻¹) and (b) G' , G'' dependence on frequency (rad s⁻¹) for 3 wt % C₁₆E₆/5 mol % C₁₆TAB/D₂O at 35 °C. (c and d) Same as parts a and b but for 50.6 wt % C₁₆E₆/D₂O at 35 °C.

minimize considerably any perturbations, inhomogeneities, and instabilities in the flow pattern.

(ii) Neutron Scattering. The SANS measurements were made on the LOQ diffractometer²⁰ at the ISIS pulsed neutron source at the Rutherford Appleton Laboratory. The measurements were made using the white beam time-of-flight method, in a scattering vector, q , range of 0.008–0.25 Å⁻¹. The measurements were all made in D₂O, and for the 10 mm path length, the sample transmission was ~50%. All of the measurements were made using a finely collimated neutron beam, using a 2 mm diameter cadmium aperture immediately before the sample cell window, and the neutron beam was incident in the x - y plane (see Figure 1). The data were corrected for detector response, the spectral distribution of the incident neutron beam, and converted to an absolute scattering cross section, $I(q)$ (in cm⁻¹), using standard procedures. Typical measurement times were ~10–20 min per position (for the 2 mm diameter beam).

(iii) Rheology Measurements. Steady and dynamic rheological measurements were performed on an ARES controlled strain rheometer (TA Instruments, New Castle, DE). A cone-and-plate system (diameter 50 mm, angle 0.04 rad) was used to carry out all of the measurements. The frequency spectra were conducted in the linear viscoelastic regime of the samples, as determined previously by dynamic strain sweep experiments. To avoid the impact of solvent evaporation, a solvent trap was used. Measurements were made at 35 °C for the 3 wt % C₁₆E₆/C₁₆TAB charged wormlike mixed micelles and at 60 °C for the 51 wt % C₁₆E₆ lamellar phase system. Temperature control

on the rheometer was achieved by a Peltier plate temperature control system. The measurements were made primarily for input into the flow profile calculations, but they also provide an important contribution to the characterization required to fully interpret the scattering data.

The results for both the 3 wt % C₁₆E₆/C₁₆TAB charged wormlike mixed micelles and the 51 wt % C₁₆E₆ lamellar phase systems are shown in Figure 2.

Figure 2a shows the viscosity and stress as a function of strain for the wormlike mixed micelles. The viscosity shows a shear thinning behavior, and the stress–strain relationship with the plateau and upturn at high shear rates is indicative of shear banding.^{21,22} The linear viscoelasticity shows a trend toward a classical maximum in G'' (see Figure 2b), but a plateau in G' is not clearly seen. Furthermore, this does not result in the expected classical semicircular Cole–Cole plot. This could be associated with the long relaxation time in the system.

The G' , G'' data for the lamellar phase show a linear viscoelastic region at low frequencies, consistent with gel-like behavior (see Figure 2c). The viscosity and stress as a function of strain rate (see Figure 2d) show a more classical behavior. However, there is a suggestion of two plateaus in the stress–strain curve, and this could be indicative of a shear induced transition.

(iv) Flow Profile Calculations. The flow profile for a Newtonian fluid has been calculated using the computational fluid dynamics package CFX (version 10), ANSYS Inc., using the Omega Reynolds stress model. The rectangular slot geometry

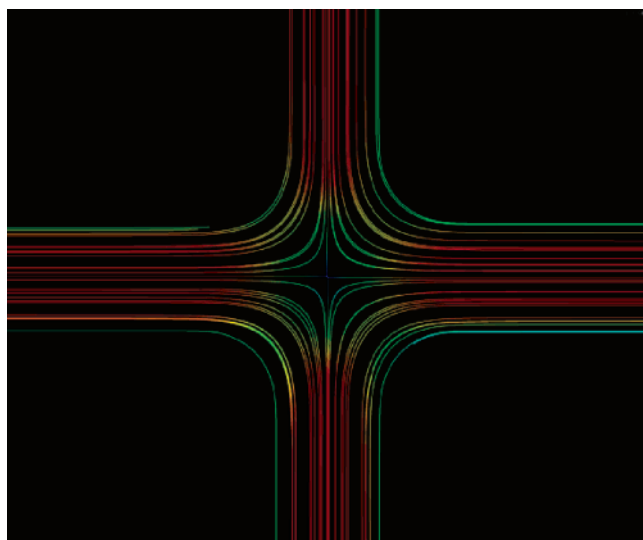


Figure 3. Calculated flow patterns for a Newtonian fluid, using the parameters described in the text.

of the cell (with input and output channels 70 mm in length and $11 \times 0.5 \text{ mm}^2$ in cross section) was recreated, and the flow profiles were modeled for a flow rate of $4.4 \text{ cm}^3 \text{ s}^{-1}$, a velocity of 8 cm s^{-1} , and a strain rate of 7.3 s^{-1} . Figure 3 shows the resulting flow pattern within the central region and in the input and output arms of the cell.

(v) Optical Birefringence Measurement. Optical texture measurements were made by illuminating the sample window with a white light source through crossed polars, and this provides a visualization of the flow pattern within the cell. Strictly, it visualizes the stress profile, and for a Newtonian fluid, this will coincide with the flow profile. This is shown in Figure 4 for both the lamellar phase dispersion of C_{16}E_6 and the mixed surfactant wormlike micelles of $\text{C}_{16}\text{E}_6/\text{C}_{16}\text{TAB}$.

For the lamellar phase dispersion of C_{16}E_6 , the local rotation of plane polarized light by the oriented lamellar domain identifies the local perturbation of solution microstructure. The flow patterns obtained are complex but reflect the local director of domains of coaligned lamellae. The symmetric nature of the pattern confirms that the opposed jet arrangement of the cell is functioning correctly. The light and dark regions can be inverted by rotating both polars simultaneously. Although quantitative analysis would require some form of calibration, in general, the greater ordering corresponds to the regions of increased optical brightness, with lamellae alignment being directly correlated with the optical director.

Figure 4 shows that in the entry and exit regions the domains are rotated and aligned along the flow direction. At the turning regions, they align with the tangent of the curve corresponding to the flow direction. In the central region, the optical rotation pattern is very narrow and is consistent with a highly confined 90° rotation of the flow at the collision point. Subsequent extraction of the flow at the top and bottom of the cells preserves this high degree of alignment in the central region. There is a dark region preceding the stagnation point which corresponds to the arresting region which precedes the stagnation point.

Similar measurements were made for samples containing charged wormlike micelles of $\text{C}_{16}\text{E}_6/\text{C}_{16}\text{TAB}$, but in this case, the exception was that the polars were uncrossed, as this gave better optical clarity. The flow pattern in the cell is again very obvious from the optical texture (see Figure 4) and is broadly consistent with predictions for a Newtonian fluid (Figure 3). This sample is highly viscoelastic and shear thinning, and the

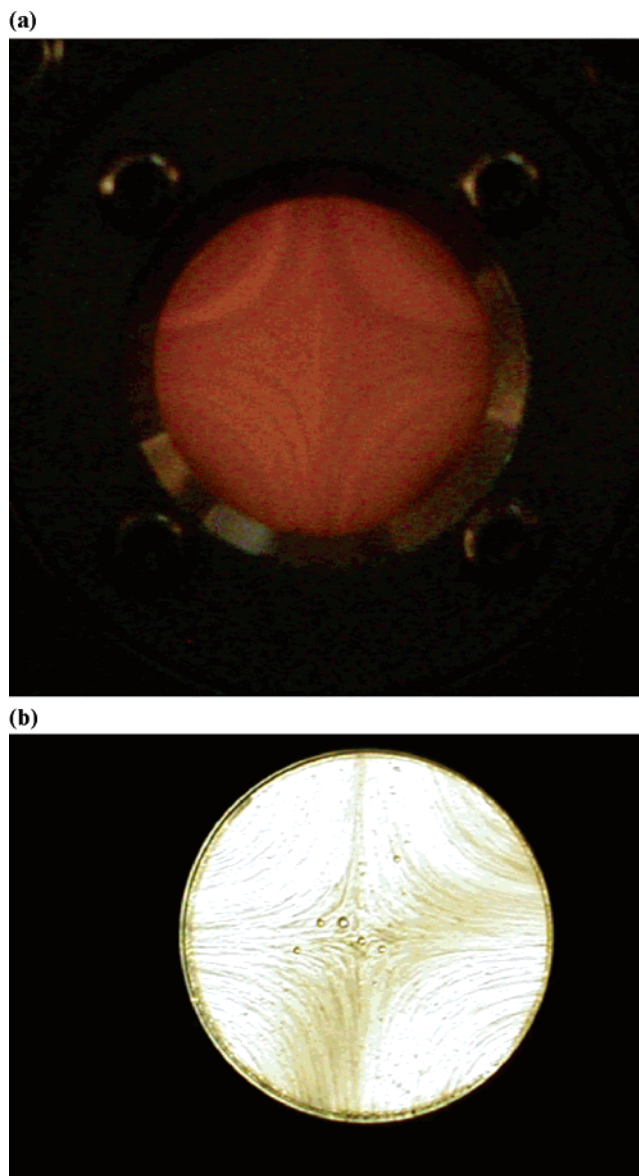


Figure 4. Optical birefringence for (a) 50.6 wt % $\text{C}_{16}\text{E}_6/\text{D}_2\text{O}$ at 35°C and (b) 3 wt % $\text{C}_{16}\text{E}_6/5 \text{ mol } \% \text{C}_{16}\text{TAB}/\text{D}_2\text{O}$ at 35°C .

coarse texture of the optical patterns obtained is an indication of the distance scale over which domains of coaligned rods persist.

(vi) Samples and Materials. Measurements were made for 3% $\text{C}_{16}\text{E}_6/5 \text{ mol } \% \text{C}_{16}\text{TAB}/\text{D}_2\text{O}$ at 35°C and for 50.6 wt % $\text{C}_{16}\text{E}_6/\text{D}_2\text{O}$. The deuterium oxide (D_2O) was supplied by Fluorochem. The C_{16}E_6 was obtained from Nikkol, and the C_{16}TAB , from Merck. The surfactants were all used as supplied. After each sample, the cell was flushed with high purity water (Elga Ultrapure).

Results and Discussion

For the two different surfactant systems, SANS measurements were made in the elongational flow cell with a 2 mm diameter beam at 2 or 3 mm intervals, from the cell center (labeled 10, 10) along the input ($y = 10$, x direction) and output ($x = 10$, y direction) directions, and at off-axial positions. Prior to this, measurements were made in the cell center (stagnation point) as a function of flow rate to determine the optimal alignment conditions for both systems.

(i) Wormlike Micelles (3% $\text{C}_{16}\text{E}_6/5 \text{ mol } \% \text{C}_{16}\text{TAB}$). Measurements were made on the wormlike mixed micellar

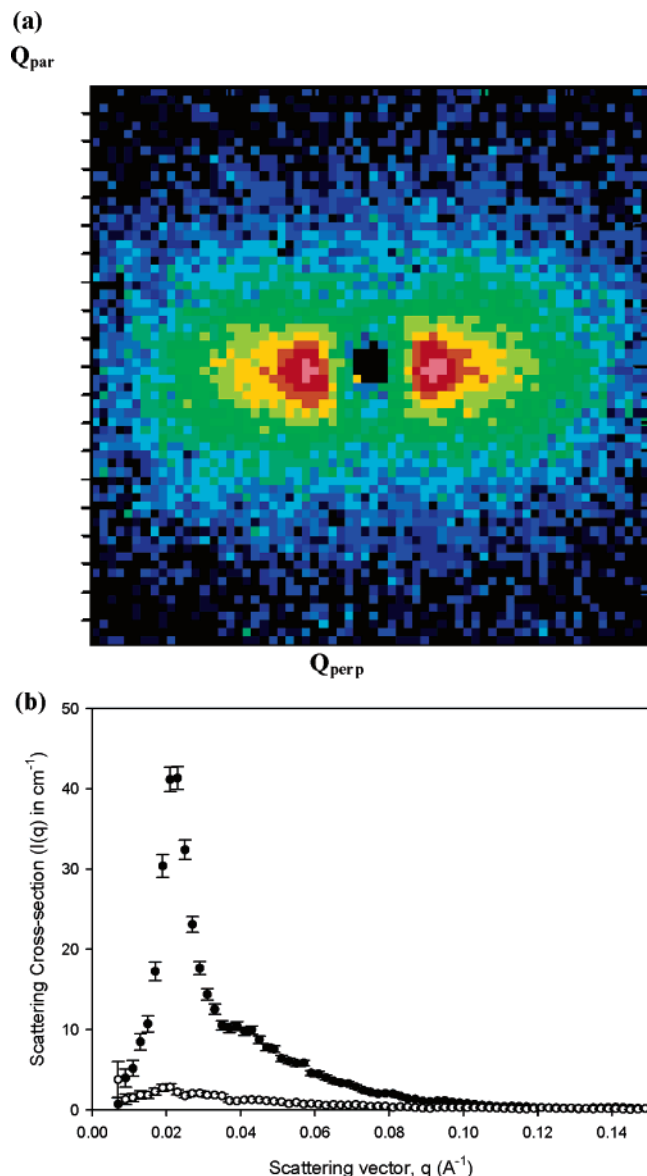


Figure 5. (a) Intensity contour map (q_{\perp} , q_{\parallel}) for 3 wt % $C_{16}E_6$ /5 mol % $C_{16}TAB/D_2O$ at 35 °C and 50 s^{-1} and at the cell center (10, 10). (b) Same as part a except intensity as a function of scattering vector, q , in the q_{\perp} (●) and q_{\parallel} (○) directions.

solution of 3 wt % $C_{16}E_6$ /5 mol % $C_{16}TAB/D_2O$ at 35 °C. The intensity contour map for the scattering at the cell center (10, 10) and at an elongational flow rate of 50 s^{-1} is shown in Figure 5a, and the q_{\perp} , q_{\parallel} intensity cuts are shown in Figure 5b.

The scattering is consistent with highly aligned interacting elongated micelles and similar to that previously reported under similar conditions²³ but under shear flow (see, for example, Figure 6 in ref 23). The data are consistent with the elongated micelles being oriented in the flow direction. Figure 6a shows the variation in the intensity contour map at the cell center (10, 10) as a function of flow rate, from 8 to 50 s^{-1} .

The anisotropy in the scattering (measured at $q \sim 0.025\text{ Å}^{-1}$, the q value of the interaction peak in the scattering), the intensity ratio in the q_{\perp}/q_{\parallel} directions, is shown in Figure 6b. With increasing flow rate, the elongated micelles become more aligned (the anisotropy increases). In addition to the increasing anisotropy in the scattering, the director (the mean direction of the orientation of the elongated micelles) oscillates about the q_x direction with increasing flow, until at the highest flow rate it is in the q_{\parallel} (q_x) direction. Elongated particles will precess

about the flow direction, with an orientation angle to that flow direction that decreases with increasing value of the ratio G/D_r for viscous shear (where G is the shear rate and D_r is the rotational diffusion coefficient). However, it is generally observed that the mean direction of orientation, even at modest shear rates, is in the flow direction. Such effects are probably masked by the broad distribution of orientations at low shear rates. However, in a different system, off-axis ordering has been reported by Brown and Rennie²⁴ for monodisperse nickel hydroxide colloidal platelets at low shear rates in a Couette flow cell. In this case, it was attributed to the effects of packing constraints in their higher volume fraction system. This is not the case here for the wormlike micelles of $C_{16}E_6/C_{16}TAB$. However, there are other possibilities for this variation in the mean director direction. This variation in the mean director orientation with flow rate could be attributed to the mixed flow regime that exists in such flow geometries. That is, although the measurements were made at the stagnation point in the cell, for this system, in addition to extensional flow, there is a small shear flow contribution, as discussed in the description of the cell shear flow. However, the optical measurements, as discussed later, are consistent with “plug” flow, and thus, such effects are expected to be minimal. The other possibility is that the variation in the director is associated with flow instabilities in the cell. In non-Newtonian fluids, like these elongated micellar structures, flow instabilities are observed.²⁵ Indeed, the rheological measurements (see earlier discussion) are consistent with the classical shear thinning systems for which “shear banding” is observed. Other flow instabilities, such as the onset of turbulence, would tend to result in a reduced alignment, and this is observed here for flow rates $>50\text{ s}^{-1}$. However, at the lower shear rates, instabilities such as vortices have been reported in such non-Newtonian systems and would be expected particularly at the input and exit regions where there are abrupt changes in the flow geometry. Here, the measurements are made at the “stagnation point” of the cell, where the flow is in its most stable configuration, and thus, the effects of flow instabilities are unlikely.

Figure 7 shows a map of the intensity contour patterns measured at 3 mm intervals across the cell, from the center along the input and output flow directions, and in off-axis positions.

On the flow axes, in the horizontal (x) and vertical (y) directions, the rods are aligned in the flow direction, with increasing orientational order along the input channel (x) to the cell center (10, 10), the stagnation point, and along the output channel (y). The off-axis scattering is consistent with reduced orientational order but shows no systematic variation in the mean director direction, except at the extreme off-axis positions (see position 5, 5 in Figure 7, for example). The reduced order is consistent with a reduced effective flow rate off-axis. This is in marked contrast to the calculated flow profiles (see Figure 3).

The alignment behavior under elongational flow is broadly similar to that observed in shear flow.²³ Although slightly different sample conditions are used here, the anisotropy in the scattering was shown to depend strongly upon temperature and the $C_{16}E_6/C_{16}TAB$ composition;²³ significant alignment is achieved at substantially lower flow rates under elongational flow.

The evolution of the anisotropy, $I(q_{\perp})/I(q_{\parallel})$, in the scattering with flow rate (see Figure 6b) shows an interesting variation, which was not previously reported for this system.²¹ At low flow rates ($<30\text{ s}^{-1}$), the change in anisotropy with flow rate is relatively modest. This may in part reflect the minor changes

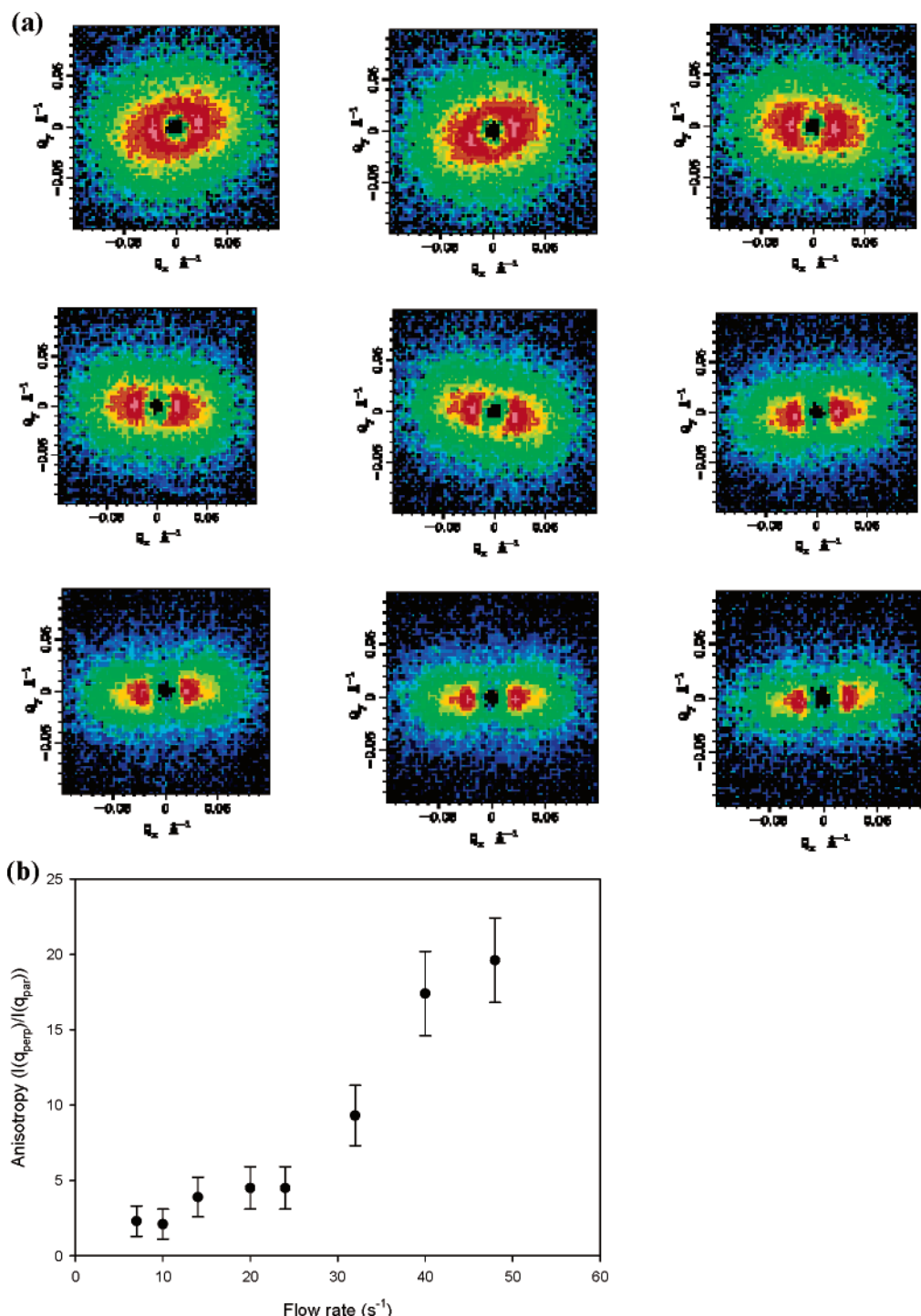


Figure 6. (a) Intensity contour maps at the cell center as a function of shear rate (7, 10, 14, 20, 24, 32, 40, and 48 s^{-1}). (b) Anisotropy, $I(q_{\perp})/I(q_{\parallel})$, at $q \sim 0.025 \text{ Å}^{-1}$ as a function of flow rate (s^{-1}).

in the director direction as it oscillates about the q_x direction. However, at $\sim 30 \text{ s}^{-1}$, the anisotropy increases markedly to approach saturation at higher flow rates. For flow rates $> 50 \text{ s}^{-1}$, the anisotropy starts to decrease, and this is associated with the onset of turbulent or chaotic flow. Similar effects have been previously reported for systems subjected to shear flow; for example, see the work of Kalus et al.²⁶ on *n*-hexadecyloctyldimethylammonium bromide micelles. A careful study at low shear rates showed a threshold for the onset of substantial alignment and was attributed to the initial weak alignment of short rodlike micelles, and the transition to larger aggregates above a threshold shear value showing strong alignment, and providing evidence of a shear induced transformation. This was

also reported by Munch et al.²⁷ in transient SANS studies of trimethyltetradecylammonium salicylate, who reported a threshold shear rate of 50 s^{-1} for a transition from short rods to highly elongated structures.

In their study of the kinetics of alignment and decay of alignment of the entangled threadlike micelles of cetyltrimethylammonium 3,5-dichlorobenzoate under shear flow, Butler et al.²⁸ in contrast provided evidence for two different alignment processes. These were attributed to an initial process involving the local deformation (stretching) of the network of highly elongated micelles, followed by a larger scale disentanglement and alignment of the individual micelles. Furthermore, under extensional flow, Odel et al.¹¹ demonstrated a similar behavior

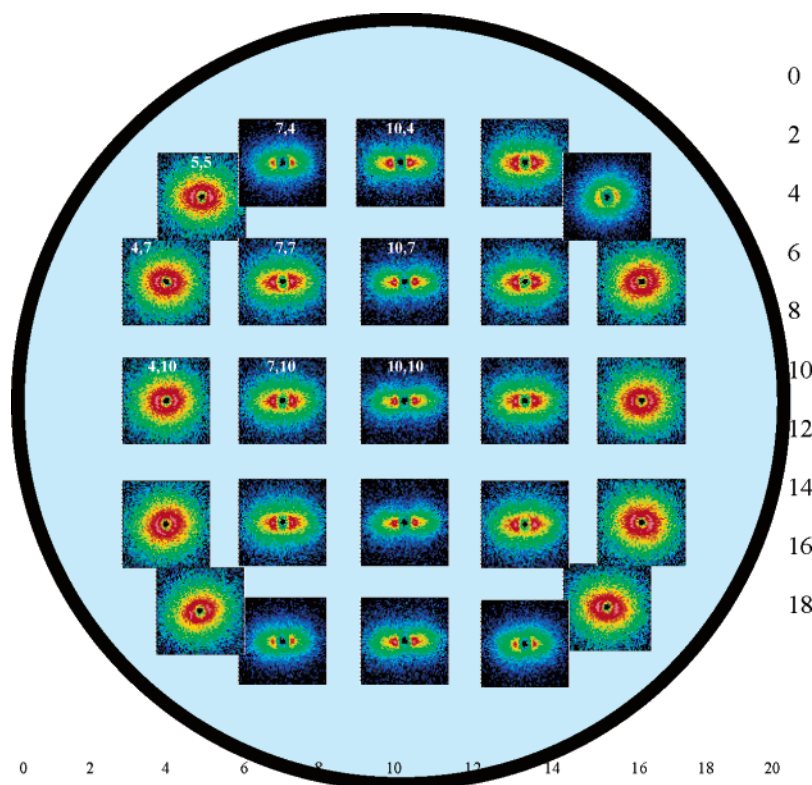


Figure 7. Same as Figure 5, but the intensity contour maps (q_{\perp} , q_{\parallel}) were measured at 3 mm intervals over the cell aperture.

in polymer solutions, where the initial anisotropy was clearly attributable to stretching and disentanglement and the subsequent increase in anisotropy was due to alignment. Hence, we attribute the variation in anisotropy with increasing flow rate to these deformation and alignment processes rather than any flow induced growth.

(ii) $C_{16}E_6$ L_{α} Lamellar Phase. Measurements were made on the L_{α} lamellar phase of the nonionic surfactant $C_{16}E_6$, for 50.6 wt % $C_{16}E_6/D_2O$ at 55 °C at a flow rate of 10 s^{-1} . Figure 8 shows the intensity contour maps (q_{\perp} , q_{\parallel}) as a function of position, measured at 2 mm intervals along the input and output channels of the flow, and at off-axis positions.

The scattering shows a highly aligned lamellar phase at low elongational flow rates, with the lamellae aligned parallel to the flow direction along the input and output directions. This is consistent with previous observations under shear flow.²⁹ The orientational order is most pronounced from the central stagnation point (10, 10) along the output flow direction (q_y), in the equivalent of the “c” orientation in the nomenclature of the recent literature. That is, the lamellar planes are oriented in the flow direction. In shear (Couette) flow, this would correspond to the lamellae being parallel to the flow–vorticity plane and perpendicular to the shear gradient direction. Off-axis and at the input to the central region, the orientational order is less pronounced, and in the off-axis positions, the orientation direction (director) rotates to reflect the mean direction of the flow pattern. This is seen more clearly in Figure 9, which shows azimuthal intensity scans around the intensity contours (at a q value corresponding to the lamellar peak at $q \sim 0.1 \text{ \AA}^{-1}$).

Figure 9a shows the azimuthal scans, measured from the entrance direction (2, 10) toward the central stagnation point (10, 10), along the x direction. This shows the increasing orientational ordering as the central stagnation point is approached and the rotation of the director (the mean orientation direction) through 90°. This should not be confused with the change in orientation from “c” to “a”, that is, from the flow–

vorticity plane to the flow–shear gradient plane observed in shear flow at higher shear rates.²⁹ Here, it is just reflecting the change in direction of the flow, from the x direction to the y direction going to the stagnation point of the cell. However, what is particularly notable is that, at intermediate positions, between the entrance (2, 10) and the center (10, 10), there is an apparent increase in disorder as the director rotates. Furthermore, close inspection of the azimuthal scans in Figure 9a shows that this is accompanied by the formation of a distinct bimodal distribution of orientations (see data for position 6, 10). This is analogous to that seen in shear flow at higher shear rates,^{29,30} where at shear rates intermediate between the transition from “c” to “a” orientation (director in flow or vorticity directions), a bimodal distribution of preferred orientations was observed. That is, in shear flow, both “a” and “c” orientations, consistent with lamellar sheets parallel to the flow–vorticity and shear gradient–flow planes, coexist. In the y direction, from the central stagnation point (10, 10) toward the output (10, 2), there is increased alignment (see Figure 9b). In this case, in this region of the elongational flow cell, there are lamellae aligned parallel to the flow direction and in the orthogonal direction. Figure 9c shows the azimuthal scans for the off-axis positions, and this illustrates in more detail how both the mean direction of the director and the degree of ordering change. In the azimuthal scans, it is seen that the mean orientation of the director changes to reflect the changes in the mean direction of flow. Furthermore, at the more extreme off-axis positions (see data for positions 4, 14 and 8, 18), the width of the distributions is much broader, corresponding to a much lower degree of ordering. The change in orientational ordering (quantified by the half width, $\Delta\varphi$, of the peaks in the azimuthal scans) goes from ~ 40 to $\sim 100^\circ$ from position 4, 12 to position 8, 18.

The variation in the orientational ordering and the direction of the director over the flow velocity pattern for the L_{α} lamellar phase of $C_{16}E_6$ is broadly similar to that reported by Idziak et al.⁵ for the SDS/pentanol/dodecane lamellar phase. The variation

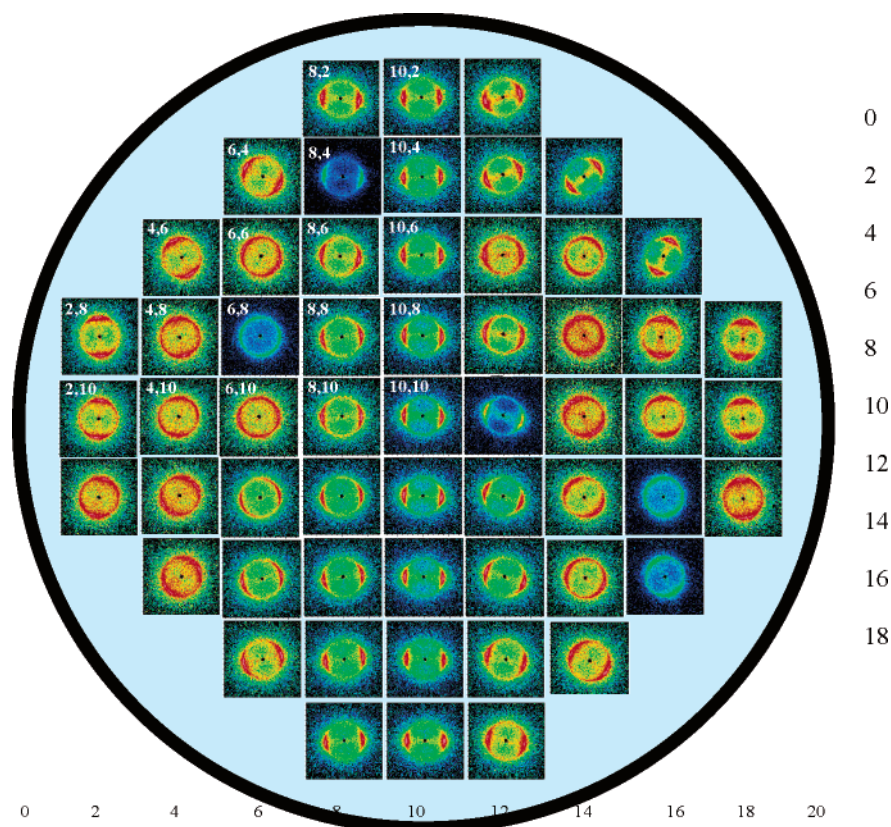


Figure 8. Intensity contour maps (q_{\perp} , q_{\parallel}) for 50.6 wt % $C_{16}E_6/D_2O$ at 55 °C and a flow rate of 10 s^{-1} , measured at 2 mm intervals over the cell aperture.

in the orientational ordering over the central region is also reproduced in the calculated flow profiles (see Figure 3).

Idziak et al.⁵ also reported a variation in the “ d ” spacing with flow rate, which was attributed to a stretching and straightening of the undulating lamellae above a critical flow rate, as predicted theoretically by Ramaswamy.³¹ This is also observed here for the $C_{16}E_6$ lamellar phase. This is shown here in Figure 10, where the change in d spacing is plotted as a function of the flow rate. The form of this variation with increasing flow rate is similar to that reported by Idziak et al.⁵ The d spacing initially decreases, and then, beyond a flow of $\sim 10\text{ s}^{-1}$, it increases to an equilibrium value that is smaller than its original value. This initial decrease is consistent with the arguments of Ramaswamy³¹ and is attributed to a stretching and straightening of the individual lamellae. However, Idziak et al.⁵ found it difficult to get quantitative agreement with the theory, and we will pursue this aspect no further. Beyond a flow rate of 10 s^{-1} , the variation in d spacing decreases and eventually reaches a more or less constant value. This was attributed to a decrease in domain size and hence due to a breaking up of membrane domains. Our measurements on $C_{16}E_6$ are not made to sufficiently low q values to get a reliable estimate of domain size, but there is other evidence in the scattering data which strongly supports that hypothesis. The anisotropy in the scattering, $I(q_{\perp})/I(q_{\parallel})$, measured at the q value corresponding to the first-order Bragg peak shows a variation which is consistent with that interpretation (see Figure 10b). At low flow rates, the anisotropy initially decreases due to reorganization effects. Beyond that, it subsequently increases, corresponding to greater flow induced ordering, and this is coincident with the region where the d spacing is decreasing most rapidly due to a stretching of the membranes. At higher flow rates, above that which corresponds to the abrupt change in the d spacing, the anisotropy starts to

decrease. This is indicative of less flow induced order, which would be a direct consequence of a reduced domain size.

(iii) General Discussion. A direct comparison with shear flow is not made in the paper, but high degrees of orientational order are observed for the lamellar system, $C_{16}E_6$, at low shear and low flow rates in both flow geometries. Hence, it is difficult to draw any specific conclusions about the relative efficiencies of the two flow regimes. However, a significant difference is that relatively high shear rates were required to induce the coexisting “c” and “a” orientations, whereas in the elongational flow cell this occurs at much lower flow rates. For the mixed surfactant wormlike micelles of $C_{16}E_6/C_{16}TAB$, comparison with previously published data for shear flow²³ is consistent with the elongational flow providing a more efficient degree of alignment. In elongational flow, the degree of orientational order is saturated at a flow rate of $\sim 50\text{ s}^{-1}$, whereas, in shear flow, it is at least an order of magnitude higher.²³

However, there is a notable difference between the intensity contour maps measured across the cell aperture for the lamellar system and the wormlike micelles, in that the degree to which the orientational director follows the flow pattern is markedly different. For the lamellar system, the director maps out the change in the flow direction across the cell, in a way similar to that observed by Idziak et al.⁵ This is consistent with the calculated flow profile for a Newtonian fluid, as shown in Figure 3, and that inferred from the birefringence measurements (see Figure 4a).

For the wormlike micelles, the optical visualization of the flow pattern is broadly similar, but the texture of the light scattering pattern is markedly different (see Figure 4b). However, the variation in the orientational ordering from the SANS measurements across the cell aperture does not reflect that flow pattern in the cell. The differences between the orientational

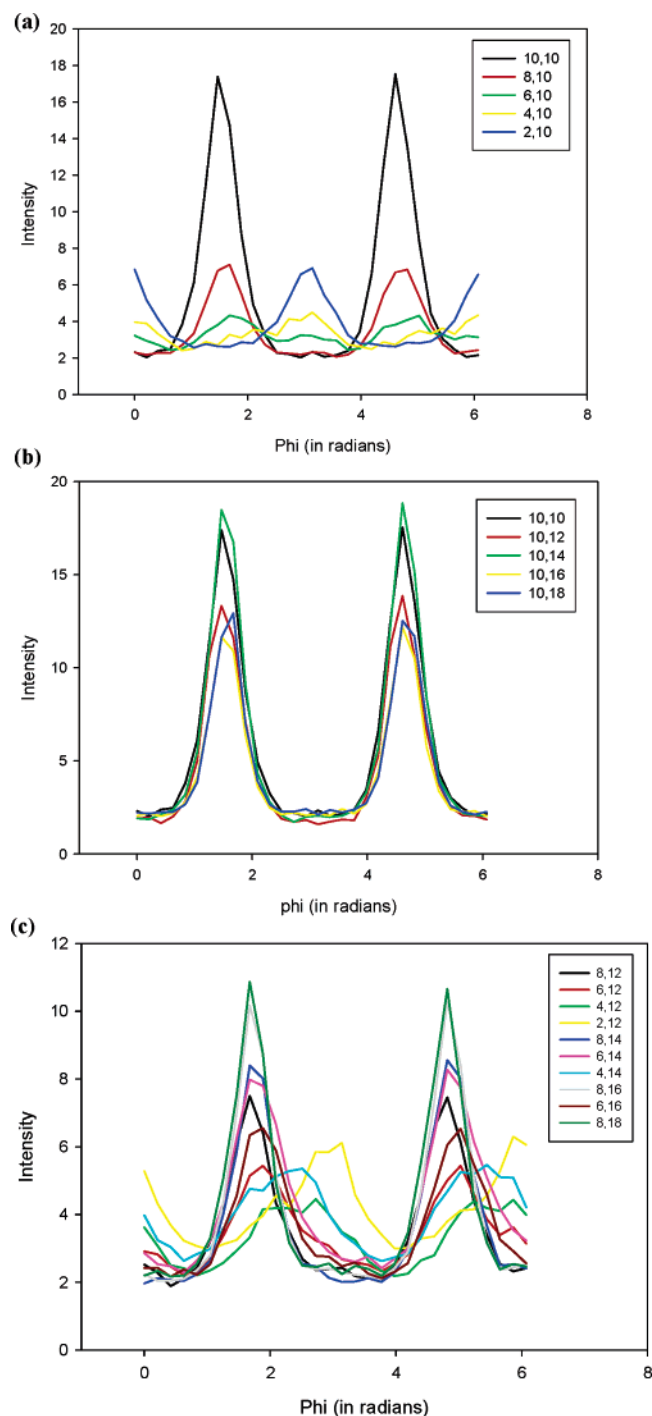


Figure 9. Azimuthal distribution of intensity, measured at $q \sim 0.1 \text{ \AA}^{-1}$ for the sample in Figure 8, and the cell positions as indicated in the figures: (a) central x axis; (b) central y axis; (c) off-axis positions.

distribution patterns observed for the lamellar phase systems and the wormlike micelles of $C_{16}E_{16}/C_{16}TAB$ originate predominantly from the differences in phase volume. The lamellar system is space filling, whereas the wormlike micelles have a lower phase volume and from the rheology measurements will be expected to exhibit shear thinning and shear banding. Hence, the wormlike micelle system can form channels within the bulk fluid where part can remain relatively static and the rest can move more freely. That is, as expected for such non-Newtonian shear thinning systems, the flow behavior is characterized by plug flow. The SANS measurements are bulk measurements, whereas the light scattering is dominated predominantly by the region in contact with the windows. Hence, for this system, it

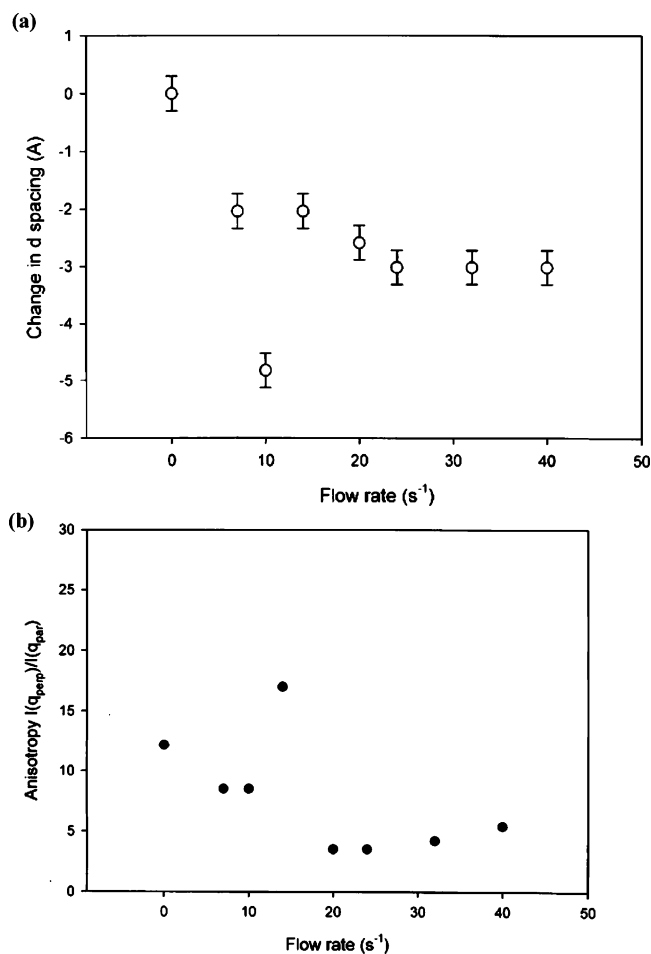


Figure 10. (a) Variation in d spacing for 50.6 wt % $C_{16}E_6/D_2O$ at 55 °C at the cell center (10, 10) as a function of flow rate (s^{-1}). (b) Variation in scattering intensity anisotropy, $I(q_{\perp})/I(q_{\parallel})$, measured at the q value corresponding to the first-order Bragg peak.

is likely, as observed here, that the SANS data and optical response are quite different.

Summary

We have described an elongational flow cell for SANS measurements, based on the crossed-slot geometry of Idziak et al.,¹⁸ and we have demonstrated how spatially resolved SANS measurements can be made with a spatial resolution of $\sim 2 \text{ mm}$. Two different surfactant systems have been studied, the charged wormlike mixed micelles of $C_{16}E_6/C_{16}TAB$ and the L_{α} lamellar phase of $C_{16}E_6$. The orientational distributions of the lamellar phase of $C_{16}E_6$ reflect and visualize the flow velocity pattern within the cell. For the L_{α} lamellar phase of $C_{16}E_6$, a bimodal distribution of orientations is observed, which is analogous to that observed in shear flow. Furthermore, variations in the lamellar d spacing and degree of alignment are attributable to a flow induced stretching of the membranes at low flow rates and the formation of smaller domains due to fracture at higher flow rates. The charged wormlike mixed micelles of $C_{16}E_6/C_{16}TAB$ show a much weaker coupling to the flow pattern, which is attributed to shear thinning and exhibits the characteristics of flow induced micellar growth.

References and Notes

- (1) Butler, P. *Curr. Opin. Colloid Interface Sci.* **1999**, *4*, 214.
- (2) Rennie, A. R.; Clarke, S. M. *Curr. Opin. Colloid Interface Sci.* **1996**, *1*, 34.

- (3) Walkenstrom, P.; Hermansson, A. M. *Curr. Opin. Colloid Interface Sci.* **2002**, *7*, 413.
- (4) Jerrard, H. G. *Chem. Rev.* **1959**, *59*, 345.
- (5) Idziak, S. H. J.; et al. *Eur. Phys. J.* **2001**, *E6*, 139.
- (6) Butler, M. F.; Donald, A. M.; Ryan, A. J. *Polymer* **1997**, *38*, 5521.
- (7) Hayter, J. B.; Penfold, J. *J. Phys. Chem.* **1984**, *88*, 4589.
- (8) Thurn, H.; Kalus, J.; Hoffman, H. *J. Chem. Phys.* **1984**, *80*, 3440.
- (9) Penfold, J.; Staples, E.; Cummins, P. G. *Adv. Colloid Interface Sci.* **1991**, *34*, 451.
- (10) Taylor, G. J. *Proc. R. Soc. London* **1934**, *A146*, 501.
- (11) Odell, J. A.; Keller, A.; Atkins, E. D. T. *Macromolecules* **1985**, *18*, 1443.
- (12) Bent, J.; et al. *Science* **2003**, *301*, 1691.
- (13) Terry, A. E.; Odell, J. A.; Nicol, R. J.; Tiddy, G. J. T.; Wilson, J. E. *J. Phys. Chem. B* **1999**, *103*, 11218.
- (14) Keller, A.; Muller, A. J.; Odell, J. A. *Prog. Colloid Polym. Sci.* **1987**, *75*, 179.
- (15) Eastman, J. R.; Goodwin, J. W.; Howe, A. M. *Colloid Surf., A* **2000**, *161*, 329.
- (16) Smitter, L. M.; Torres, M. E.; Muller, A. J.; Saez, A. E. *J. Colloid Interface Sci.* **2001**, *244*, 164.
- (17) Odell, J. A.; Keller, A.; Rubin, Y. *J. Chem. Phys.* **1988**, *88*, 4027.
- (18) Kisilak, M.; Anderson, H.; Babcock, N. S.; Stetzer, M. R.; Idziak, S. H. J.; Sirota, E. B. *Rev. Sci. Instrum.* **2001**, *72*, 4305.
- (19) Muller, N.; Burghammer, M.; Riekel, C. *Nucl. Instrum. Methods* **2001**, *467*, 858.
- (20) Heenan, R. K.; King, S. M.; Penfold, J. *J. Appl. Crystallogr.* **1997**, *30*, 1140.
- (21) Cates, M. E.; Candau, S. J. *J. Phys: Condens. Matter* **1990**, *2*, 6969.
- (22) Spenley, N. A.; Cates, M. E.; McLeish, T. C. B. *Phys. Rev. Lett.* **1993**, *71*, 939.
- (23) Cummins, P. G.; Penfold, J.; Staples, E. *Langmuir* **1992**, *8*, 31.
- (24) Brown, A. B. D.; Rennie, A. R. *Phys. Rev. E* **2000**, *62*, 851.
- (25) Wheeler, E. K.; Fischer, P.; Fuller, G. G. *J. Non-Newtonian Fluid Mech.* **1998**, *75*, 193.
- (26) Kalus, J.; Hoffmann, H.; Chen, S. H.; Lindner, P. *J. Phys. Chem.* **1989**, *93*, 4267. Jindal, V. K.; Kalus, J.; Pils, H.; Hoffmann, H.; Lindner, P. *J. Phys. Chem.* **1990**, *94*, 3129.
- (27) Munch, C.; Hoffmann, H.; Ibel, K.; Kalus, J.; Neubauer, G.; Schueizer, U.; Selbach, J. *J. Phys. Chem.* **1993**, *97*, 4314.
- (28) Butler, P. D.; Magid, L. J.; Hamilton, W. A.; Hayter, J. B.; Hammouda, B.; Kreke, P. *J. Phys. Chem.* **1996**, *100*, 442.
- (29) Penfold, J.; Staples, E.; Lodhi, A. K.; Tucker, I.; Tiddy, G. J. T. *J. Phys. Chem. B* **1997**, *101*, 66.
- (30) Zipfel, J.; Berghausen, J.; Lindner, P.; Richtering, W. *J. Phys. Chem. B* **1999**, *103*, 2841.
- (31) Ramaswamy, S. *Phys. Rev. Lett.* **1992**, *69*, 112.